Biomedical Optics EXPRESS

Handheld, rapidly switchable, anterior/posterior segment swept source optical coherence tomography probe

Derek Nankivil,[1,*] Gar Waterman,[1] Francesco LaRocca,[1] Brenton Keller,[1] Anthony N. Kuo,[2] and Joseph A. Izatt[1,2]

[1]*Department of Biomedical Engineering, Duke University, Durham, NC, 27708, USA*
[2]*Department of Ophthalmology, Duke University Medical Center, Durham, NC, 27710, USA*
[*]*derek.nankivil@duke.edu*

Abstract: We describe the first handheld, swept source optical coherence tomography (SSOCT) system capable of imaging both the anterior and posterior segments of the eye in rapid succession. A single 2D microelectromechanical systems (MEMS) scanner was utilized for both imaging modes, and the optical paths for each imaging mode were optimized for their respective application using a combination of commercial and custom optics. The system has a working distance of 26.1 mm and a measured axial resolution of 8 μm (in air). In posterior segment mode, the design has a lateral resolution of 9 μm, 7.4 mm imaging depth range (in air), 4.9 mm 6dB fall-off range (in air), and peak sensitivity of 103 dB over a 22° field of view (FOV). In anterior segment mode, the design has a lateral resolution of 24 μm, imaging depth range of 7.4 mm (in air), 6dB fall-off range of 4.5 mm (in air), depth-of-focus of 3.6 mm, and a peak sensitivity of 99 dB over a 17.5 mm FOV. In addition, the probe includes a wide-field iris imaging system to simplify alignment. A fold mirror assembly actuated by a bi-stable rotary solenoid was used to switch between anterior and posterior segment imaging modes, and a miniature motorized translation stage was used to adjust the objective lens position to correct for patient refraction between −12.6 and + 9.9 D. The entire probe weighs less than 630 g with a form factor of 20.3 x 9.5 x 8.8 cm. Healthy volunteers were imaged to illustrate imaging performance.

OCIS codes: (110.4500) Optical coherence tomography; (170.4460) Ophthalmic optics and devices; (080.3620) Lens system design; (170.0110) Imaging systems; (170.5755) Retina scanning; (170.4470) Ophthalmology.

References and links

1. S. Radhakrishnan, A. M. Rollins, J. E. Roth, S. Yazdanfar, V. Westphal, D. S. Bardenstein, and J. A. Izatt, "Real-time optical coherence tomography of the anterior segment at 1310 nm," Arch. Ophthalmol. **119**(8), 1179–1185 (2001).
2. "*http://optovue.com/products/ivue/*.
3. W. Jung, J. Kim, M. Jeon, E. J. Chaney, C. N. Stewart, and S. A. Boppart, "Handheld optical coherence tomography scanner for primary care diagnostics," IEEE Trans. Biomed. Eng. **58**(3), 741–744 (2011).
4. "*http://www.bioptigen.com/products/c-class/*.
5. F. LaRocca, D. Nankivil, S. Farsiu, and J. A. Izatt, "Handheld simultaneous scanning laser ophthalmoscopy and optical coherence tomography system," Biomed. Opt. Express **4**(11), 2307–2321 (2013).
6. C. D. Lu, M. F. Kraus, B. Potsaid, J. J. Liu, W. Choi, V. Jayaraman, A. E. Cable, J. Hornegger, J. S. Duker, and J. G. Fujimoto, "Handheld ultrahigh speed swept source optical coherence tomography instrument using a MEMS scanning mirror," Biomed. Opt. Express **5**(1), 293–311 (2014).
7. R. L. Shelton, W. Jung, S. I. Sayegh, D. T. McCormick, J. Kim, and S. A. Boppart, "Optical coherence tomography for advanced screening in the primary care office," J. Biophotonics **7**(7), 525–533 (2014).
8. F. LaRocca, D. Nankivil, S. Farsiu, and J. A. Izatt, "True color scanning laser ophthalmoscopy and optical coherence tomography handheld probe," Biomed. Opt. Express **5**(9), 3204–3216 (2014).

#249401 Received 3 Sep 2015; revised 15 Oct 2015; accepted 16 Oct 2015; published 21 Oct 2015

9. A. H. Dhalla, D. Nankivil, and J. A. Izatt, "Complex conjugate resolved heterodyne swept source optical coherence tomography using coherence revival," Biomed. Opt. Express **3**(3), 633–649 (2012).
10. D. Nankivil, A.-H. Dhalla, N. Gahm, K. Shia, S. Farsiu, and J. A. Izatt, "Coherence revival multiplexed, buffered swept source optical coherence tomography: 400 kHz imaging with a 100 kHz source," Opt. Lett. **39**(13), 3740–3743 (2014).
11. A. H. Dhalla, D. Nankivil, T. Bustamante, A. Kuo, and J. A. Izatt, "Simultaneous swept source optical coherence tomography of the anterior segment and retina using coherence revival," Opt. Lett. **37**(11), 1883–1885 (2012).
12. T. Klein, W. Wieser, C. M. Eigenwillig, B. R. Biedermann, and R. Huber, "Megahertz OCT for ultrawide-field retinal imaging with a 1050 nm Fourier domain mode-locked laser," Opt. Express **19**(4), 3044–3062 (2011).
13. A. V. Goncharov and C. Dainty, "Wide-field schematic eye models with gradient-index lens," J. Opt. Soc. Am. A **24**(8), 2157–2174 (2007).
14. D. A. Atchison and G. Smith, "Chromatic dispersions of the ocular media of human eyes," J. Opt. Soc. Am. A **22**(1), 29–37 (2005).
15. Laser Institute of America, American National Standard for Safe Use of Lasers ANSI Z136.1–2007 (American National Standards Institute, Inc., 2007).
16. P. Thévenaz, U. E. Ruttimann, and M. Unser, "A pyramid approach to subpixel registration based on intensity," IEEE Trans. Image Process. **7**(1), 27–41 (1998).
17. S. J. Chiu, X. T. Li, P. Nicholas, C. A. Toth, J. A. Izatt, and S. Farsiu, "Automatic segmentation of seven retinal layers in SDOCT images congruent with expert manual segmentation," Opt. Express **18**(18), 19413–19428 (2010).
18. F. LaRocca, S. J. Chiu, R. P. McNabb, A. N. Kuo, J. A. Izatt, and S. Farsiu, "Robust automatic segmentation of corneal layer boundaries in SDOCT images using graph theory and dynamic programming," Biomed. Opt. Express **2**(6), 1524–1538 (2011).

1. Introduction

As optical coherence tomography (OCT) develops into an important tool for anterior segment characterization, the ability to use a single instrument for both anterior and posterior segment imaging may become a desirable feature for clinical systems. Several commercial ophthalmic OCT systems are capable of switching between anterior and posterior imaging modes; however, this requires the addition or removal of optics from the sample path and adjustment of the reference path. In addition, most of these systems require a patient that is cognizant and capable of sitting upright in a standard ophthalmic patient positioner, requirements which may not be realistic for a young child or an elderly patient.

To mitigate some of these constraints, researchers have developed handheld OCT instruments [1–8]. A few of these instruments are capable of imaging both the anterior and posterior segment [2–4, 7], but switching between modes requires the operator to remove and/or add an additional lens or lens system. This distracts the operator from the patient and requires realignment with the patient eye after switching modes.

Previously, we reported on the application of coherence revival to create an extended depth (complex conjugate resolved) heterodyne swept source OCT (SSOCT) system without the use of acousto-optic or electro-optic modulators [9]. We used efficient sweep buffering along with coherence revival and polarization-based spatial multiplexing to quadruple the effective speed of an SSOCT system [10]. Also, we used coherence revival and polarization-based multiplexing to create a heterodyne SSOCT system capable of imaging both the anterior and posterior eye simultaneously [11]. The form factor of this system made it impossible to use as a handheld and difficult to integrate with a standard slit lamp patient positioner and chin rest. This system also utilized a variable optical delay line and did not share a common objective lens. In addition, the simultaneous use of two beams reduced the sensitivity of each image by 6 dB. With these limitations in mind, we have designed an SSOCT system that is rapidly switchable between anterior and posterior imaging modes with a single handheld microelectromechanical systems (MEMS)-based optical probe and a common objective lens. The system was used to image the cornea and retina of healthy human volunteers.

#249401 Received 3 Sep 2015; revised 15 Oct 2015; accepted 16 Oct 2015; published 21 Oct 2015

2. Methods

The handheld anterior/posterior segment SSOCT probe was designed to meet the following general performance specifications: 1) sequentially image the anterior or posterior segment with < 1 s delay when switching modes, 2) incorporate an iris camera to simplify alignment, and 3) weigh less than 900 g with a minimal device form factor. The optical design performance specifications for the posterior segment system were: 1) permit diffraction limited imaging of the human retina across a 15° field of view (FOV), 2) compensate for patient refractive errors ranging from −12 to + 9 D, and 3) have a > 20 mm working distance from the eye. The optical design performance specifications for the anterior segment system were: 1) permit diffraction limited imaging of the human cornea across a 10 mm square FOV, 2) have an object side telecentricity better than 1°, as indicated by the ray angle of incidence at the object plane, 3) provide a depth of focus (DOF) of more than 3 mm to permit imaging of deeper structures, and 4) have a > 20 mm working distance from the eye. The following subsections describe how we addressed these goals through the optical and mechanical design of the SSOCT engine and the handheld probe.

2.1 Swept source optical coherence tomography engine

An SSOCT system (Fig. 1) with a spectrally balanced interferometer topology [12] was constructed using a frequency swept laser (AXP50124-3, Axsun Technologies Inc., Billerica, MA) with a central wavelength of 1040 nm, a 100 nm bandwidth, and a 100 kHz sweep rate.

Detection and digitization of the OCT signal was achieved using an AC coupled dual balanced receiver with a 1 GHz bandwidth (PDB481C-AC, Thorlabs Inc., Newton, NJ) and a 12-bit 1.8 GS/s digitizer (ATS9360, Alazar Technologies Inc., Pointe-Claire, QC, Canada), respectively. All of the hardware was controlled using custom graphics processing unit (GPU)-accelerated software written in C++ to provide real-time display of OCT images. The reference mirror and lens were mounted on a high speed translation stage (A-LSQ075D-E01, Zaber Technologies Inc., Vancouver, BC).

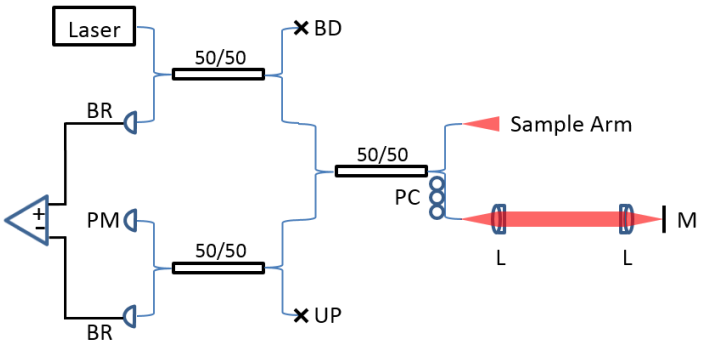

Fig. 1. SSOCT system with spectrally balanced topology. BR: balanced receiver. PM: power meter. BD: beam dump. UP: unused port. PC: polarization controller. L: lens. M: mirror.

2.2 Optical design

The optical design of the sample arm is shown in Fig. 2. The optics were optimized in optical design software, Zemax (Radiant ZEMAX LLC, Redmond, WA), using an eye model with a gradient index lens [13]. The eye model was modified as described in [8] with glass types adjusted to match human ocular dispersion [14]. A gimbal-less two-axis scanning MEMS micromirror (13Z1.1, Mirrorcle Technologies Inc., Richmond, CA) was used to control beam position on the subject eye. An achromatic lens (45785, ⌀ = 6 mm, P = 66.6 D, Edmund Optics Inc., Barrington, NJ) was used as a collimator to produce a 2.4 mm beam diameter.

#249401 Received 3 Sep 2015; revised 15 Oct 2015; accepted 16 Oct 2015; published 21 Oct 2015

For the posterior segment design, a telescope with unity magnification was constructed using off-the-shelf lenses with an effective focal length of 37 mm. Achromatic doublet lenses were used to reduce chromatic aberration and lens splitting, with a 3-to-5 ratio in refractive power, was used to minimize spherical aberration. Specifically, each low power doublet (AC254-100-C, ⌀ = 25.4 mm, P = 10.0 D, Thorlabs Inc., Newton, NJ) was paired with a high power doublet (⌀ = 25.4 mm, P = 16.7 D, Thorlabs Inc., Newton, NJ). The posterior segment design was then used to constrain the optimization of the anterior segment design.

In an effort to minimize the size of the probe, telecentric scanning of the anterior segment was achieved by adding optical elements through a short fold mirror assembly while maintaining a common objective lens for both designs (anterior and posterior segment). The cost function for the optical design optimization was restricted by fixing the position of the posterior segment lenses while adjusting a fold mirror assembly and a lens system to obtain a telecentric focal plane at the cornea. To this end, a custom matched achromatic pair (⌀ = 20.0 mm, P = 18.7 D) was designed with consideration for manufacturability by using test plates and common Ohara (Ohara Corp., Branchburg, NJ) glasses available at Optimax (Optimax Systems Inc., Ontario, NY). A tolerance stack analysis was performed to ensure that the optical design was sufficiently resilient to meet the specifications given common commercial fabrication tolerances.

In addition, non-sequential optical models were created to perform Monte-Carlo simulations of the infrared (IR) (λ = 850 ± 22 nm) light emitting diode (LED) (HIR7393C, Everlight Electronics Co., New Taipei City, Taiwan) illumination used in the wide-field iris imaging system. The angle of incidence of 4 LEDs arranged circumferentially around the objective was adjusted to optimize the uniformity in the plane of the cornea. The collection path takes advantage of an intermediary image plane by using a dichroic mirror to pass the image relayed by the anterior segment optics to a large sensor CMOS camera (MQ042RG-CM, Ximea Corp., Golden, CO). This camera has the smallest form factor of all of the large sensor cameras at 26 x 28 x 18 mm, which worked well for integration into the handheld probe. The wavelengths used matched a dichroic coating design available at Chroma (ZT970spxxr, Chroma Technologies Corp., Bellows Falls, VT) so that only the substrate needed customization. Control of the intensity of the illuminator was achieved via pulse-width modulation with a custom external dimming circuit.

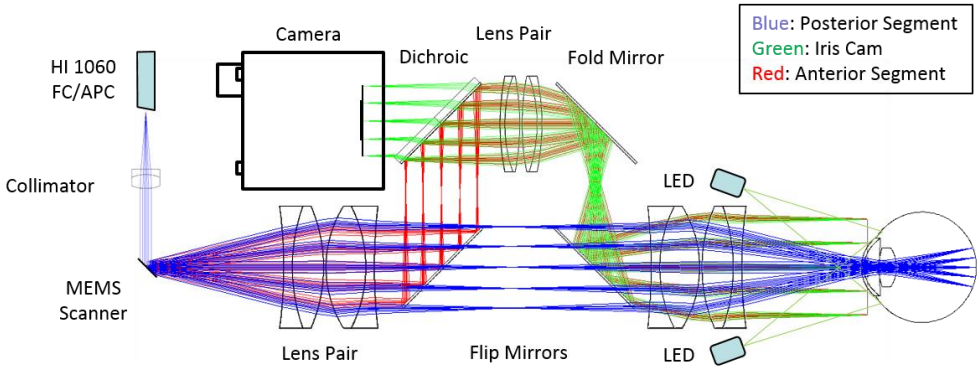

Fig. 2. Handheld probe optical design: blue, red, and green rays depict the posterior segment, anterior segment and iris camera collection paths, respectively.

The optical performances of both the anterior and posterior segment system designs are shown in Fig. 3. The system has a working distance of 26.1 mm. Diffraction limited performance was achieved in the optical design, giving a predicted lateral resolution (Airy radius) of 8.6 μm and a radial FOV of 22° (15.4° square FOV) for the posterior segment

#249401 Received 3 Sep 2015; revised 15 Oct 2015; accepted 16 Oct 2015; published 21 Oct 2015

design. The anterior segment system has a lateral resolution (Airy radius) of 25.1 µm, a DOF of 3.6 mm, and a 17.5 mm radial FOV (12.4 mm square FOV).

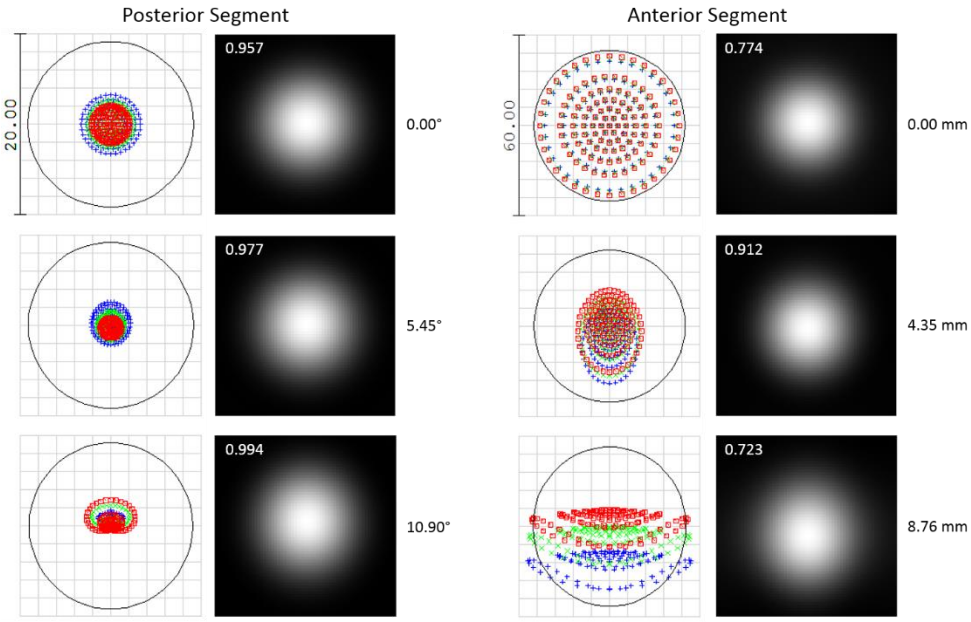

Fig. 3. Spot diagrams and Huygens point spread functions (PSFs) for the posterior (left) and anterior segment (right) SSOCT illumination spanning radial field angles of 0.00, 5.45 and 10.90°. Spot diagrams are color coded for 3 wavelengths spanning the bandwidth of the source and the scale is 20 and 60 µm in the posterior and anterior segment spot diagrams, respectively. The Strehl ratio is shown in the upper left of each PSF plot. A field angle of 10.90° corresponds to a radial FOV of 21.8° (square FOV of 15.4°) for the posterior segment system and a radial FOV of 17.5 mm (square FOV of 12.4 mm) for the anterior segment system. Both the posterior and anterior segment systems are diffraction limited at 8.6 and 25.1 µm, respectively (airy disk is shown by black circle on spot diagrams).

2.3 Mechanical design

The optical design for the probe was used to specify component locations in the mechanical design. The mechanical design for the system was developed in Solidworks (Dassault Systemes, Solidworks Corp., Waltham, MA) and is shown without the outer casing in Fig. 4. Custom lens tubes, lens spacers, and mirror mounts were designed and fabricated to accommodate the closely spaced optics of the system and to maintain a small footprint. The internal skeleton and other structural components were made of aluminum to simplify fabrication and to maintain a low weight. The use of undersized dowel pins along with a tightly toleranced skeleton provided for accurate component positioning, while the use of tangential and toroidal interfaces on pertinent lens surfaces minimized stress induced distortions of the optical wavefront. Zemax was used to determine the maximum permissible positional error of optical components. A mechanical tolerance stack analysis was performed to ensure that the optical design specifications were satisfied given standard commercial mechanical fabrication tolerances. The lens pair closest to the eye was mounted on a miniature motorized translation stage (MM-3M-EX, National Aperture Inc., Salem, NH) with a total travel of 25.4 mm to allow for refraction correction from −12.6 to + 9.9 D. A bistable rotary solenoid (RSR14/10-CAB0, Takano Co., Kamiina-gun, Nagano, Japan) was used to provide the ability to toggle between measurement modes (anterior and posterior) by flipping two fold mirrors. The motion systems and functional components of the probe are illustrated in Visualization 1. The probe enclosure design was iterated based on input and feedback from

#249401 Received 3 Sep 2015; revised 15 Oct 2015; accepted 16 Oct 2015; published 21 Oct 2015

an ophthalmic surgeon with the objective of improving ergonomics and optimizing rotational inertia, weight, and center of mass position of the assembled probe. The enclosure was 3D printed (Objet350 Connex, Stratasys Ltd., Edina, MN) from a rigid opaque photopolymer (VeroWhitePlus RGD875, Stratasys Ltd., Edina, MN) and consisted of two halves that were joined during assembly and secured with six low profile set screws and hex nuts. The enclosure was mated to the skeleton of the probe with two socket head cap screws. Tightly toleranced shoulders on the inside of the enclosure prevented movement of the enclosure with respect to the skeleton. The probe within its enclosure is shown in Fig. 5 in handheld operation. The handheld probe weighed 630 g and was 20.3 cm long x 9.5 cm wide x 8.8 cm tall.

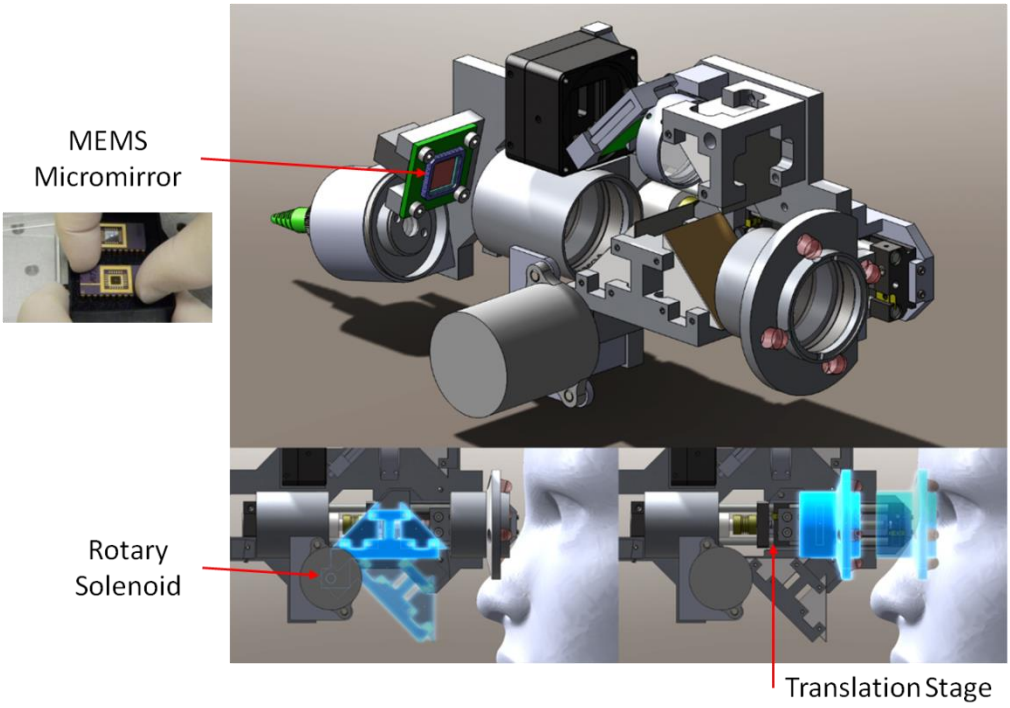

Fig. 4. Renderings of the handheld probe optomechanical design. Dimensions: 20.3 x 9.5 x 8.8 cm. (top) Isometric view. (bottom left) Switchable fold mirror assembly and (bottom right) adjustable objective motion systems are indicated with semi-transparency and a blue luminescent tone. Red arrows indicate the location of each motion system. The motion systems and functional components of the probe are illustrated in Visualization 1.

#249401 Received 3 Sep 2015; revised 15 Oct 2015; accepted 16 Oct 2015; published 21 Oct 2015

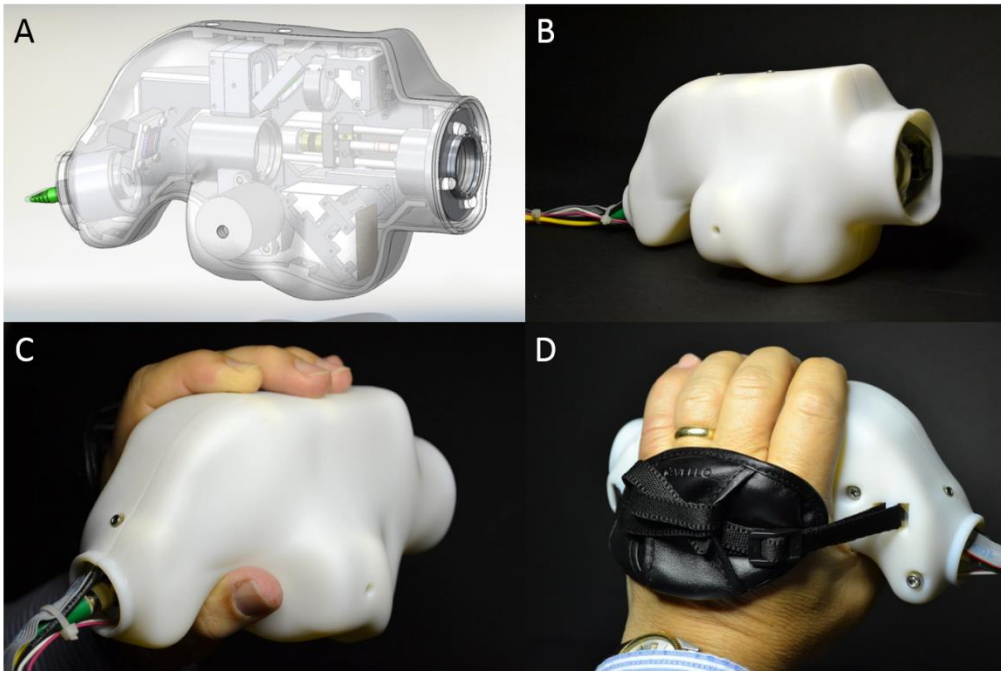

Fig. 5. Handheld SSOCT probe. (A) Isometric view of a computer aided design model of the probe inside its enclosure with the male half of the enclosure rendered as translucent to show the probe internals. (B) Same view shown in (A) of the fabricated probe in its enclosure. (C, D) Back-right and back-left views, respectively, of the probe in its enclosure during handheld operation.

2.4 Distortion correction (dewarping)

The voltage-angle response of the MEMS micromirror was nonlinear at the manufacturer-specified maximum scan rate of 100Hz. A 20 x 20 mm low reflection grid target with 0.5 mm separation between dots and 0.25 mm dot diameters (62951, Edmund Optics Inc., Barrington, NJ) was used to assess the distortion in both anterior and posterior segment imaging modes and in the iris camera view. An optical path length (OPL) matched eye phantom (45792, ⌀ = 12 mm, P = 49.9 D, OPL = 31.7 mm, Edmund Optics Inc., Barrington, NJ) was used to focus the posterior segment beam onto the target. SSOCT volumes consisted of 1000 A-scans per B-scan with 256 B-scans per volume. Summed voxel projections (SVPs) were rendered to visualize 2D images of the grid targets. A distortion correction process was developed as shown in Fig. 6. Thresholding and blob centroid detection were used to find the center of each dot. Dot locations were then used to create a least-squares, piecewise linear transform to dewarp the image. Separate transforms were used to dewarp each imaging mode and field of view. The effective imaging range was determined by the area within the transformed image containing dot locations around the border of the image, which slightly reduced the FOV to 22.4° (13.3 x 14.9°) for the posterior segment system and 18.1 mm (12 x 13.5 mm) for the anterior segment system.

#249401 Received 3 Sep 2015; revised 15 Oct 2015; accepted 16 Oct 2015; published 21 Oct 2015

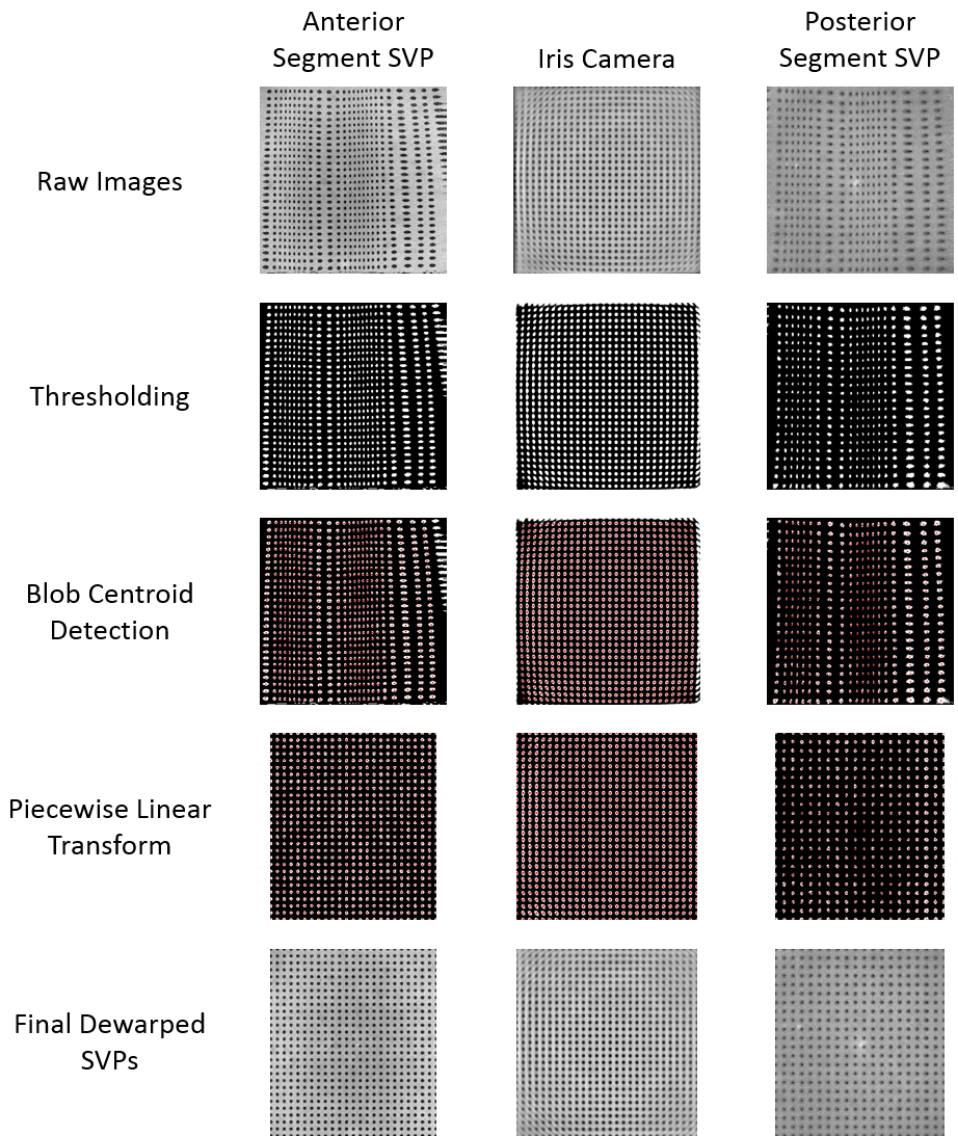

Fig. 6. Distortion correction. (top) Raw images of the grid target were thresholded (upper middle) and the blob centroids (shown in red) were automatically detected (middle). The dot locations were used to create a least-squares piecewise linear transform to dewarp the image as shown by the thresholded (lower middle) and final dewarped images (bottom). The left, center and right columns indicate images acquired in the anterior, iris camera, and posterior segment imaging modes, respectively.

2.5 Ethical considerations

The use of the experimental setup for *in vivo* measurements in humans was approved by the Duke University Hospital System Institutional Review Board and adhered to the tenets of the Declaration of Helsinki. Informed consent was obtained from each subject. Subjects had no known pathology and consisted of a 24 year old male myope (–5.5 D), a 26 year old male emmetrope, a 28 year old female myope (–3 D), a 32 year old male myope (–5 D), and a 35 year old male myope (–2.25 D).

#249401 Received 3 Sep 2015; revised 15 Oct 2015; accepted 16 Oct 2015; published 21 Oct 2015

3. Results

Peak sensitivity and sensitivity fall-off profiles were measured for each channel of the sample arm (Fig. 7). The peak sensitivity was 99 and 103 dB for the anterior and posterior segment channels, respectively. The difference in sensitivity is partly due to the slightly lower collection efficiency of the anterior segment system (which has ten additional optical elements), and partly due to the required use of two different reflection phantoms for the anterior and posterior imaging mode sensitivity measurements. The fall-off was characterized using a Gaussian fit of the peak intensity of each A-scan. For the posterior segment channel, we observed a −6dB imaging range of 4.9 mm in air (3.7 mm in tissue). For the anterior segment channel, we observed a −6dB imaging range of 4.5 mm in air (3.4 mm in tissue). The axial resolution was essentially constant over the imaging range with a mean full width at half maximum of ~8 μm (in air) for both systems.

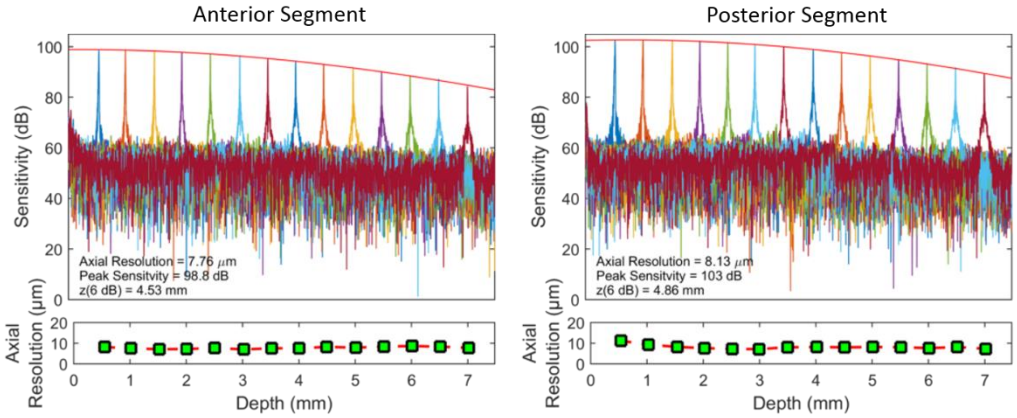

Fig. 7. Sensitivity fall-off of the anterior (left) and posterior segment (right) sample arms. A-scans are color coded by optical path length difference.

When switching between modes, both the flip mirror and the reference arm require actuation. Adjustment of the reference arm was achieved in 40 ms with the use of a high-speed stage such that the flip mirror system was the limiting factor dictating the time required to switch modes. Measurements of the temporal response of the flip mirror were used to determine the settling time required between switching modes (anterior/posterior segment mode) such that beam positional error from vibration induced by the mechanical action of switching was restricted to less than ½ of an Airy radius of the focused beam (Fig. 8). A camera was used to image the beam when changing modes. One hundred thirty-five experiments were performed in each mode. The images were thresholded and the centroid of the beam was determined for each frame. The mean final position of the beam across all experiments was determined and referenced as the set point. The displacement (over time) between the set point and the beam centroid positions was calculated. Then, the time to settle to within ½ an Airy radius of the set point was determined for each experiment. In 95% of the experiments the beam settled to within ½ an Airy radius of the set point in less than 0.3 and 0.37 seconds for retinal and anterior modes, respectively.

#249401 Received 3 Sep 2015; revised 15 Oct 2015; accepted 16 Oct 2015; published 21 Oct 2015

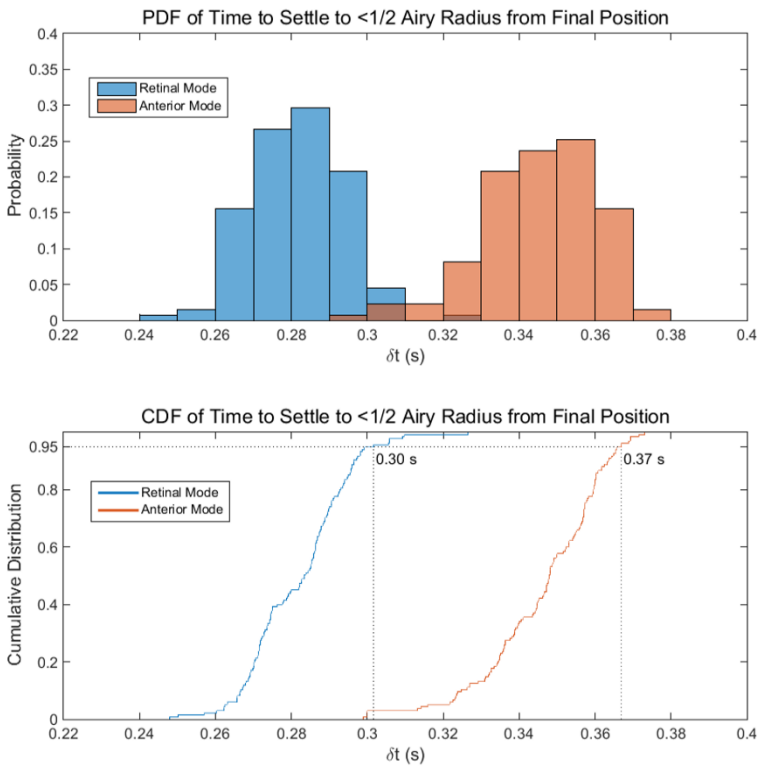

Fig. 8. (top) Probability distribution function (PDF), and (bottom) cumulative distribution function (CDF) of the flip mirror response time as indicated by the time to settle to within ½ an Airy radius of the resting position for the posterior (blue) and anterior (red) segment imaging modes.

The efficacy of the dewarping algorithm was assessed using the known spacing of the low reflectance grid target. The centroids of the dots on the edge of the central horizontal and vertical rows of the target were used as references to calculate the error of the other dot positions in both the x- and y-directions before and after dewarping (Fig. 9). The root mean squared (RMS) error after dewarping was much less than one pixel in the x- and y-directions for the posterior segment, iris camera and anterior segment systems.

#249401 Received 3 Sep 2015; revised 15 Oct 2015; accepted 16 Oct 2015; published 21 Oct 2015

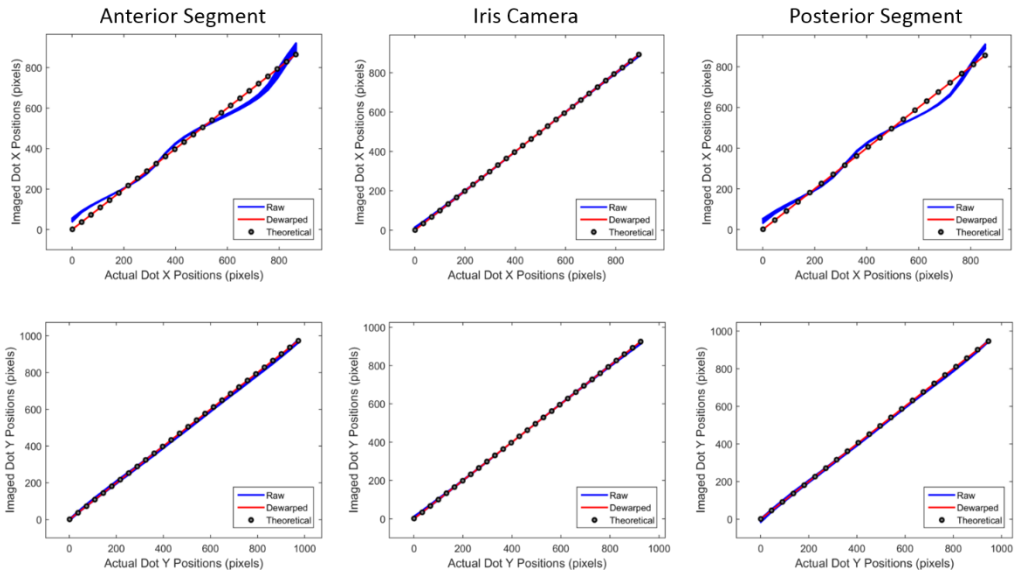

Fig. 9. Measured dot centroids as a function of actual dot positions of the grid target for all lines in the x- (top) and y-directions (bottom) for the anterior segment (left), iris camera (middle), and posterior segment (right). The mean RMS error after dewarping across all three modalities was significantly less than one pixel.

All of the hardware was controlled using custom GPU-accelerated software written in C++/CUDA to provide real-time display of OCT images, and a custom GPU-enabled ray-casting algorithm was used to enhance volume visualization. To demonstrate the applicability of dual depth SSOCT in vivo, anterior segment and retinal images were acquired from healthy volunteers (Fig. 10). All 5 subjects were successfully imaged, and the results presented herein for one subject were typical of those obtained from the others.

Before each imaging session, the fiber polarization controllers were adjusted to optimize signal while imaging a test target in anterior segment mode. The optical power output of the probe was measured with a calibrated power meter while in posterior segment mode to ensure compliance with the ANSI Z136.1 standard [15]. The power spectral density of the source, measured with an optical spectrum analyzer (Agilent 86142B, Agilent Technologies Inc., Santa Clara, CA), was used to determine the source-specific maximum permissible exposure. The optical power incident on the subject cornea was 1.7 mW, which is within the most conservative limits of the ANSI Z136.1 standard [15] for the 1040 ± 50 nm source used over a duration of up to 8.33 hours.

At the start of each imaging session, the pupil camera was used to guide the operator to nominally align the probe with the subject eye and the final alignment was achieved with the aid of real-time display of the OCT images. The pupil camera functions only in anterior segment mode. Although a pupil camera would be useful during posterior segment mode as well, we elected to omit this functionality as part of the trade-off needed to achieve the small form factor that permitted handheld operation. During anterior segment imaging, the position of the focal plane was set near the posterior cornea in order to improve corneal signal at the cost of decreased signal from the crystalline lens. Given this configuration and the limited 3.6 mm DOF (in air) of the anterior segment objective, the contrast of the crystalline lens is relatively low. For each subject, the scan protocol included a total of 8 acquisitions, 2 per mode, each consisting of 256 B-scans. The protocol proceeded as follows: anterior segment B-scans, anterior segment volume, posterior segment B-scans, and posterior segment volume. Then, the proceeding 4 steps were repeated to obtain a total of 8 acquisitions. The total recorded imaging time was 40.8 seconds, which took approximately 5 minutes per subject

#249401 Received 3 Sep 2015; revised 15 Oct 2015; accepted 16 Oct 2015; published 21 Oct 2015

when taking setup, alignment and data storage into account. Separate dispersion compensation parameters were applied to the two data sets. All images were dewarped using the method described in section 2.4. OCT B-scan images were registered using an image processing program, ImageJ (National Institutes of Health, Bethesda, MD), with the StackReg plugin [16]. OCT volumes were registered by applying previously described automatic segmentation algorithms using graph theory and dynamic programming [17, 18] to extract the top layer of the retina or cornea followed by cross correlation of the segmentations to determine axial motion.

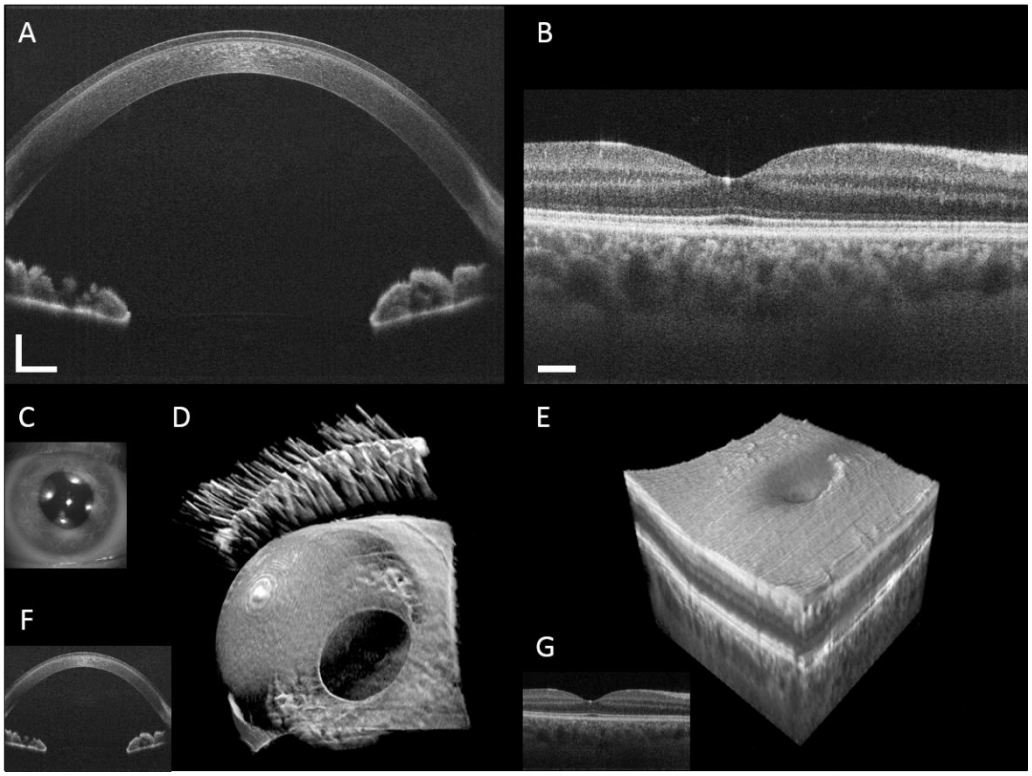

Fig. 10. Anterior segment and retinal images from a healthy volunteer. B-scan images were registered and averaged 5 times, and comprise 1376x1000 pixels for the anterior segment (A) and retina (B). For each imaging mode, averaged B-scans were taken from within a single data set. The scale bars are 1 mm (lateral) x 0.5 mm (axial) and 1° for the anterior and posterior segment B-scans, respectively. An image from the iris camera of the same subject is shown in (C). Volume visualization of the anterior (D) and posterior (E) segments comprised 1376x1000x256 voxels and was rendered in less than the data acquisition time using a custom GPU-enabled enhanced ray-casting algorithm. The volume and B-scan acquisition times were 5.1 s and 20 ms respectively. Single unaveraged B-scans of the anterior segment (F) and retina (G) selected from the volume data sets are also shown.

4. Conclusion

We have demonstrated a MEMS-based handheld dual depth SSOCT system that enables rapid, sequential imaging of the anterior segment and retina. To aid alignment, the probe includes a wide-field iris imaging system consisting of a high-resolution camera, a custom dichroic mirror, and an IR LED-based annular illumination system. A moveable fold mirror assembly, actuated by a bi-stable rotary solenoid, was used to switch between the anterior and posterior segment measurement modes, and a miniature motorized linear translation stage was used to adjust the objective position to correct for patient refractive error. Healthy volunteers were imaged to illustrate imaging performance.

#249401 Received 3 Sep 2015; revised 15 Oct 2015; accepted 16 Oct 2015; published 21 Oct 2015

Acknowledgments

This research was supported by the U.S. Army Medical Research and Material Command (USAMRMC Award # W81XWH-12-1-0397) and the Fitzpatrick Foundation Scholar Award (DN). We would like to thank Christian Viehland for his contribution of the ray-casting algorithm. Parts of this paper were presented as a talk at SPIE Photonics West, BiOS, San Francisco CA, Feb 2015, and at ARVO Annual Meeting, Denver CO, May 2015.

#249401 Received 3 Sep 2015; revised 15 Oct 2015; accepted 16 Oct 2015; published 21 Oct 2015